AGU PUBLICATIONS

Water Resources Research

RESEARCH ARTICLE

10.1002/2014WR016454

Key Points:
- A new finite water-content vadose zone solver was validated using column data
- The new method is efficient, robust, and guaranteed to conserve mass
- The new method is as accurate as the numerical solution of the Richards equation

Correspondence to:
F. L. Ogden,
fogden@uwyo.edu

Citation:
Ogden, F. L., W. Lai, R. C. Steinke, and J. Zhu (2015), Validation of finite water-content vadose zone dynamics method using column experiments with a moving water table and applied surface flux, *Water Resour. Res.*, *51*, doi:10.1002/2014WR016454.

Received 23 SEP 2014
Accepted 17 MAR 2015
Accepted article online 24 MAR 2015

© 2015. American Geophysical Union. All Rights Reserved.

Validation of finite water-content vadose zone dynamics method using column experiments with a moving water table and applied surface flux

Fred L. Ogden[1], Wencong Lai[1], Robert C. Steinke[1], and Jianting Zhu[1]

[1]Department of Civil and Architectural Engineering, University of Wyoming, Laramie, Wyoming, USA

Abstract Data from laboratory experiments on a 143 cm tall and 14.5 cm diameter column, packed with Wedron sand with varied constant upper boundary fluxes and water table velocities for both falling and rising water tables are used to validate a finite water-content vadose zone simulation methodology. The one-dimensional finite water-content Talbot and Ogden (2008) (T-O) infiltration and redistribution method was improved to simulate groundwater table dynamic effects and compared against the numerical solution of the Richards equation using Hydrus-1D. Both numerical solutions agreed satisfactorily with time series measurements of water content. Results showed similar performance for both methods, with the T-O method on average having higher Nash-Sutcliffe efficiencies and smaller absolute biases. Hydrus-1D was more accurate in predicting deponding times in the case of a falling water table, while Hydrus-1D and the T-O method had similar errors in predicted ponding times in the case of a rising water table in six of nine tests. The improved T-O method was able to predict general features of vadose zone moisture dynamics with moving water table and surface infiltration using an explicit, mass-conservative formulation. The advantage of an explicit formulation is that it is numerically simple, using forward Euler solution methodology, and is guaranteed to converge and to conserve mass. These properties make the improved T-O method presented in this paper a robust and computationally efficient alternative to the numerical solution of the Richards equation in hydrological modeling applications involving groundwater table dynamic effects on vadose zone soil moistures.

1. Introduction

Understanding of water flow in vadose zone, also called the unsaturated zone, is critical to understand interactions between surface water and saturated groundwater. Vadose zone flow is complicated due to nonlinearities and hysteresis of unsaturated hydraulic properties, and by near-surface water table dynamics. Understanding of vadose zone dynamics due to a moving water table is important, as it affects vadose zone storage capacity. *Childs and Poulovassilis* [1962] computed the steady state moisture profile above a constant speed falling water table in the case of constant rate of infiltration. Experiments were conducted to show the good agreement between computed and observed moisture profiles for falling water tables when the limiting condition was satisfied. *Childs and Poulovassilis* [1962] only performed experiments in the case of a falling water table to avoid the confounding effects of hysteresis. *Watson and Awadalla* [1985, 1986] developed equations to model drainage under moving water table conditions based on *Green and Ampt* [1911]-type approach. *Hinz* [1998] investigated the influence of periodic water table motion on water flow at the interface of the unsaturated/saturated zone, using a numerical solution of the Richards equation. The numerical solutions showed that moisture content and pressure profiles exhibited sharper fronts for water table upward movement than downward movement. *Lehmann et al.* [1998] observed strong hysteresis effects near a fluctuating capillary fringe with different flux and pressure boundary conditions, and water content varied more in the case of slow fluctuation. *Schmutz and Namikas* [2013] measured the surface moisture content above an oscillating water table and simulated the response of surface water content to water table oscillation using the Hydrus-1D program [*Simunek et al.*, 2009] with both hysteresis and nonhysteresis approaches. Comparisons between measured and simulated surface water content showed that hysteresis exerts significant influence on surface moisture content dynamics, especially when the water table is close to land surface. *Cartwright* [2014] showed evidence of hysteresis at longer oscillation periods with a sand column tests on the soil moisture-pressure dynamics above an oscillating water table.

The *Richards* [1931] equation (RE) for variably saturated soil water flow is still the most rigorous way to describe interaction between unsaturated and saturated zones [*Panday and Huyakorn*, 2004; *Simunek et al*., 2009; *He et al*., 2008]. Numerical solution of the RE is computationally expensive due to its highly nonlinear nature [*van Dam and Feddes*, 2000], required high vertical resolution on the order of mm to dm to correctly model land-surface partitioning [*Downer and Ogden*, 2004b; *Vogel and Ippisch*, 2008]. Furthermore, the RE can exhibit difficulties with numerical convergence near saturation [*Vogel et al*., 2000]. Quasi three-dimensional models with coupled one-dimensional vertical flow in the vadose zone and two-dimensional horizontal flow in the saturated zone are widely used in hydrological models, such as SHE [*Abbott et al*., 1986], GSSHA [*Downer and Ogden*, 2004a], and SWAP [*van Dam et al*., 2008].

Talbot and Ogden [2008] proposed a new one-dimensional infiltration and capillary redistribution method (T-O method) using a finite water-content formulation. The finite water-content discretization is different from the "bundle of tubes" analogy, in that all of the $\Delta\theta$ "bins" in the finite water-content discretization are in intimate contact with each other and fully interacting. The T-O method does not require spatial discretization, employs an explicit finite-volume solution of an ordinary differential equation, and is therefore unconditionally mass conservative. Comparisons against the Richards equation solution on 11 USDA soil types showed that the T-O method is capable of providing accurate estimates of infiltration rates in the case of a deep well-drained soil during multiple infiltration periods [*Talbot and Ogden*, 2008]. The [*Talbot and Ogden* 2008] infiltration methodology, improved and coupled with the finite water-content groundwater dynamics method described in this paper, was tested using time series of rainfall on 12 soil textures and found to correlate well with the RE solution [*Ogden et al*., 2015].

In this paper, soil moisture dynamics due to water table motion were studied experimentally and the results were used to validate the improved T-O method revised to simulate groundwater table dynamics as well as infiltration, and compared against the numerical solution of the Richards equation using Hydrus-1D. The experimental apparatus and experiment was fashioned after the study by *Childs and Poulovassilis* [1962].

2. Experimental Apparatus

The schematic diagram of the experimental apparatus is shown in Figure 1. The test cylinder consisted of an optically clear acrylic tube 143 cm in height with 14.5 cm inside diameter. The column was instrumented with eight Time Domain Reflectrometry (TDR) probes to monitor changes in soil moisture content. The TDR probes were installed at 15 cm intervals starting 5 cm below the sand surface and measured using a Campbell Scientific (CSI) TDR100 reflectrometer with a CSI SDMX50 multiplexer. Three absolute pressure transducers connected to 1 bar capillary suction porous ceramic cups were colocated with the second, third, and sixth TDR probes (i.e., 20, 35, and 80 cm below the sand surface) to measure the capillary head. A gage pressure transducer was installed at the bottom of the column to measure the total head at that location. A type-K thermocouple was installed in the inlet port of the column to measure the water temperature entering or exiting the column. Barometric pressure was measured using a Vaisala PTB101B pressure transmitter. The column rested upon a load cell to measure the total weight of the column. The TDR100, pressure sensors, load cell, barometer, and thermocouple were connected to a Campbell Scientific CR1000 data logger, with measurements taken at 20 second intervals. All cables and hoses were provided strain relief so as to apply a constant weight to the column.

The sand used in the column test section was Wedron 410 sand produced by Fairmount Minerals of Wedron, Illinois. This sand is 99.65% silica and has a median grain size by weight of 250 μm and a grain size range from 80 to 400 μm. Packing the column involved the following steps. First, the empty column was placed on a vibrating table. A gravel pack filter consisting of first pea gravel, then coarse sand was placed in the bottom 14 cm of the column. The oven dry Wedron sand was next packed by continuously pouring the sand at a rate of approximately 50 g s^{-1} through two 6 mm sieves into the column, all while resting on the vibrating table. Three packings were required to obtain a column with stable properties upon testing with water. Between packings the sand was removed and oven dried. The experiments reported in this paper were all performed on the same packed column.

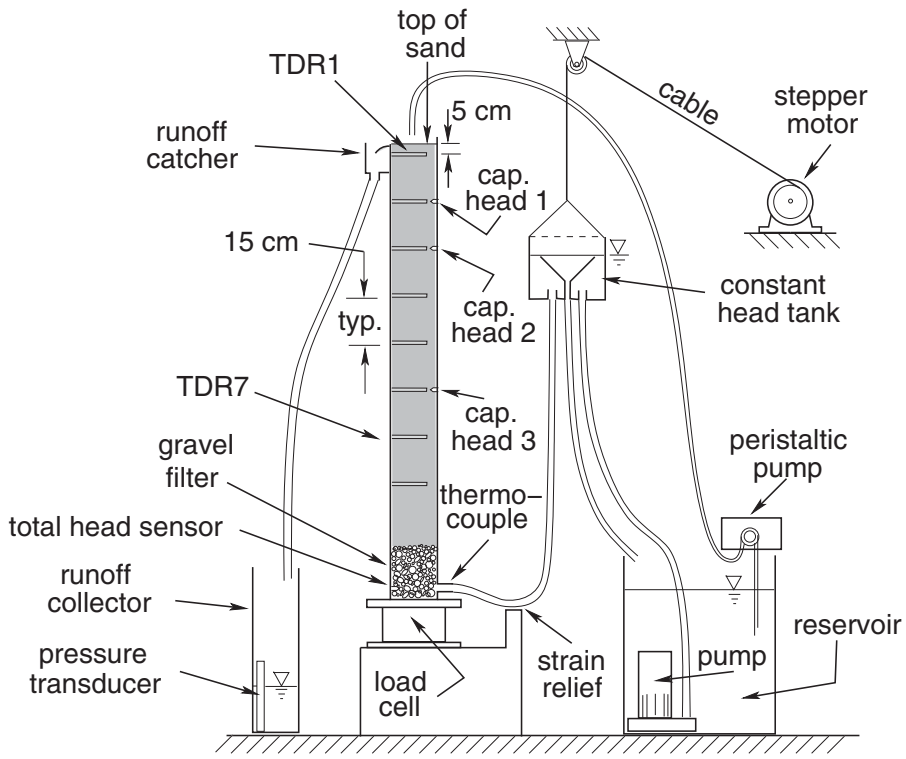

Figure 1. Schematic of experimental apparatus.

After *Childs and Poulovassilis* [1962], a constant input flux was applied to the sand surface using a peristaltic pump, which was calibrated using a stopwatch, 1000 mL beaker, and bench top scale with 0.1 g accuracy. The top of the column was covered with plastic with a vent hole to minimize evaporation, and the experiment was carried out at 25 $\pm$ 1°C. The water pressure at the bottom of the sand column was established using a constant-head tank fed by continuous flow pumped from a 150 L reservoir using a submersible pump. Flexible 12 mm inside diameter tubing with strain relief connected the constant head tank to the bottom of the column. The constant-head tank was connected using a 3 mm steel cable to a 150 mm spool on a stepper motor with 25,000 steps per revolution. This stepper motor was controlled via a LabView computer program that provided the flexibility to vary the water table velocity and to automatically start and stop water table motion while unattended. The elevation of the water surface in the constant head tank moved in the range of 20–142 cm above the bottom of the column, with 142 cm being the same elevation as the sand surface. Surface runoff of applied water during ponding was diverted into a collector, and the water level in the collector was monitored using In Situ Level TROLL 500 pressure transducer with integral data logger, which collected data at 1 min intervals. This allowed identification of ponding and deponding times with 1 min precision.

In each test, the head tank was raised to the highest position over a period of about 8 h and the sand column was naturally saturated, which caused some air to be trapped in the column. TDR measurements indicated that water content at natural saturation was very nearly 0.285, while the calculated porosity of the column was 0.311. After *Childs and Poulovassilis* [1962] a constant flux of water was applied at the sand surface during each test. Then the water table was moved downward with constant velocity for the full range of 122 cm. The constant head tank then remained at the lowest position for about 12 h before moving upward with the same velocity used before.

Tested input fluxes at the upper boundary were 0.04, 0.08, 0.13, and 0.27 of the saturated hydraulic conductivity K_s (L T^{-1}). Tests in our apparatus with input fluxes of 0.27 K_s were affected by difficulties in air entry/exit, and the results were poorly simulated by both Hydrus-1D and the T-O method. We therefore have therefore discarded those experimental results as unusable and influenced by differences between our column and the column

Table 1. Experimental Test Matrix[a]

	Applied Water Flux		
Water Table Velocity	2.36 cm h^{-1} (0.039 K_s)	4.71 cm h^{-1} (0.079 K_s)	7.59 cm h^{-1} (0.127 K_s)
13.2 cm h^{-1} (0.22 K_s)	Test 1	Test 4	Test 7
27.6 cm h^{-1} (0.46 K_s)	Test 2	Test 5	Test 8
55.2 cm h^{-1} (0.92 K_s)	Test 3	Test 6	Test 9

[a]Fluxes and water table velocities expressed in cm h^{-1} and relative to K_s (60 cm h^{-1}).

used by *Childs and Poulovassilis* [1962], which was perforated and immersed in fluid in contrast to our totally enclosed column. *Childs and Poulovassilis* [1962] tested water table velocities of 0.22, 0.46, and 0.92 of K_s. The actual values used in our test matrix are listed in Table 1, based on a measured $K_s = 60$ cm h^{-1} for the Wedron sand used (S. Jones, personal communication 2013).

3. Numerical Simulations

Laboratory measurements of vadose zone water dynamics were used to test an improved one-dimensional *Talbot and Ogden* [2008], abbreviated as T-O, finite water-content infiltration method. In the T-O method, the soil is assumed homogeneous and incompressible in layers. The finite water-content discretization showing the vadose zone above a water table is shown in Figure 2. The z axis is the depth below the sand surface, positive downward, and the horizontal axis is water content θ discretized into N constant size "bins" of uniform width $\Delta\theta$ between residual water content θ_r and effective porosity θ_e. In this study, $N = 200$ was sufficient to describe the dynamics of the system. *Lai et al*. [2015] have shown that when coupling with simpler infiltration schemes such as the Green and Ampt with Redistribution (GAR) method [*Ogden and Saghafian*, 1997], as few as 10 bins are sufficient to simulate the effect of groundwater table dynamics on infiltration fluxes.

General soil water retention and unsaturated hydraulic conductivity relations are required in the T-O method, just as with the numerical solution of the *Richards* [1931] partial differential equation. These values are calculated once for the right-edge of each finite water-content bin once at the beginning of a simulation and stored. Hydraulic conductivity and moisture retention characteristics are often described by soil characteristic models such as *Brooks and Corey* [1964] model or *Van Genuchten* [1980] model. The *Brooks and Corey* [1964] model is

$$S_e(\theta) = \frac{\theta - \theta_r}{\theta_e - \theta_r} = \left\{ \begin{array}{ll} (\psi/\psi_b)^{-\lambda}, & \psi < \psi_b \\ 1, & \psi \geq \psi_b \end{array} \right\}, \qquad (1)$$
$$K(\theta) = K_s S_e^{3+2/\lambda}$$

where θ, θ_e, and θ_r are the volumetric water content (L^3 L^{-3}), water content at effective saturation (L^3 L^{-3}), and residual water content (L^3 L^{-3}), respectively, $S_e(\theta)$ is the degree of saturation (0–1), ψ_b is the air entry value or bubbling pressure (L), ψ is the soil capillary pressure (<0), λ is dimensionless pore size distribution index parameter, and $K(\theta)$ is the unsaturated hydraulic conductivity (L T^{-1}). The *Van Genuchten* [1980] model is

$$S_e(\theta) = \frac{\theta - \theta_r}{\theta_e - \theta_r} = \frac{1}{(1 + (\alpha\psi)^n)^m}$$
$$K(\theta) = K_s S_e^{0.5} \left[1 - \left(1 - S_e^{1/m} \right)^m \right]^2, \qquad (2)$$
$$m = 1 - 1/n, \quad n > 1$$

where α is related to the inverse of air entry suction (L^{-1}), n and m are dimensionless empirical curve fitting parameters.

The derivation of the finite water-content equation in the improved T-O formulation that allows calculation of the effect of water table motion on the vadose zone water contents is given in Appendix A. The equation describing the movement of a groundwater wetting front in bin j is (from equation (A13))

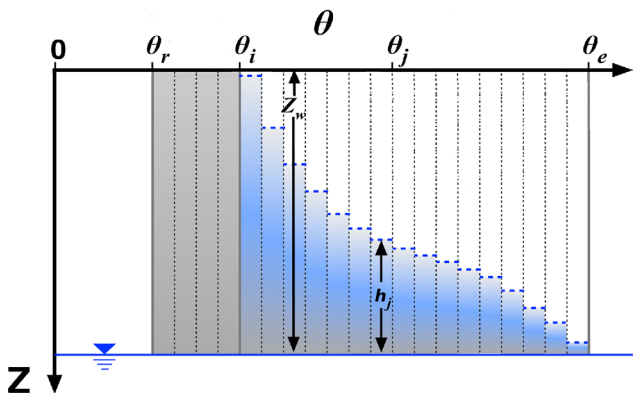

Figure 2. Discretized water content domain in the improved T-O method.

$$\frac{dh_j}{dt} = \frac{K(\theta_j) - K(\theta_i)}{\theta_j - \theta_i}\left(\frac{|\psi(\theta_j)|}{h_j} - 1\right), \tag{3}$$

where h_j is the height of the groundwater wetting front in bin j (L), dh_j/dt is the front velocity (LT^{-1}), θ_i is the water content of the right-most bin that is fully saturated from the groundwater table to the land surface, θ_j is the water content of bin j, $K(\theta_i)$ and $K(\theta_j)$ are the unsaturated hydraulic conductivities of the θ_i and θ_j bins, respectively (LT^{-1}), and $\psi(\theta_j)$ is the capillary pressure head of jth bin (L). If this distance is less than the equilibrium hydrostatic capillary head, ($h_j < |\psi(\theta_j)|$), the groundwater wetting front will move upward. Otherwise the groundwater wetting front will move downward.

In our experimental setup, the capillarity of the soil in the vicinity of the groundwater table is influenced by the applied surface flux. This was accounted for using equation (B4) that was derived in Appendix B and compared against another more complex analytical solution in equation (B5) [*Zhu and Mohanty*, 2002] in Figure B1.

Because of the rapid increase in $K(\theta)$ as the soil reaches saturation, it is common that water on the right side of the profile will advance faster than water to the left in the case of a rising water table. This can result in a condition shown in the upper portion of Figure 3. The capillary-weighted redistribution scheme employed in *Talbot and Ogden* [2008] moved water vertically in the profile and was incorrect. Our intention in simulating capillary relaxation is that it is a zero-dimensional free-energy minimization process involving only changes in interfacial energy, not potential energy. Capillary relaxation produces no advection beyond the REV scale [*Mobius et al*. 2012]. In practice, any water in bins that does not have water in the bin immediately to the left is moved to the left as far as possible. This capillary relaxation algorithm involves sorting of the bin depths from deepest to shallowest going from left to right and is used here for both the surface wetting fronts and the groundwater wetting fronts resulting in the condition shown in the lower portion of Figure 3 and can result in sharper fronts in the case of a rising water table [*Hinz*, 1998].

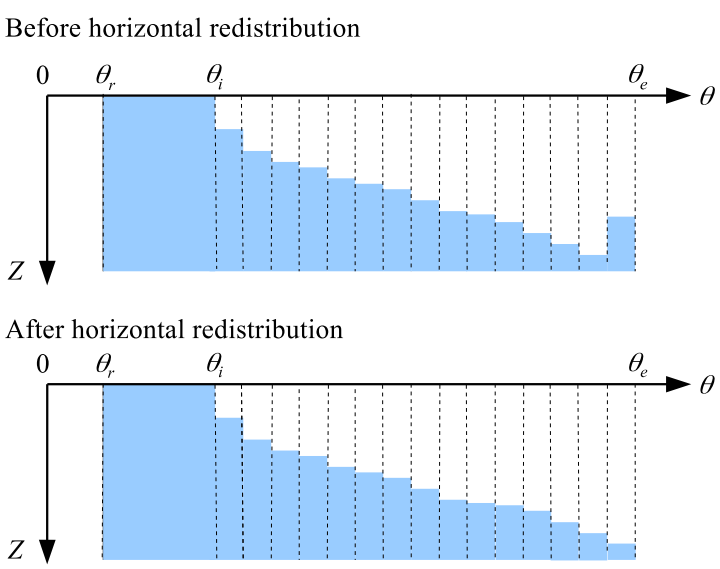

Figure 3. Surface wetting front profiles before and after capillary relaxation.

4. Results and Discussion

Figure 4 shows measured dynamic water content profiles captured when the constant head tank was 92 cm below the sand surface for each of the 18 tests (nine up and nine down). Each water content profile was drawn by connecting TDR measurements from seven TDRs. The bottom TDR, number 8, developed a leak inside the cable which rendered it inoperative for all tests. We stopped the leak and discontinued use of that TDR probe. The implications on our data collection were inconsequential, as TDR

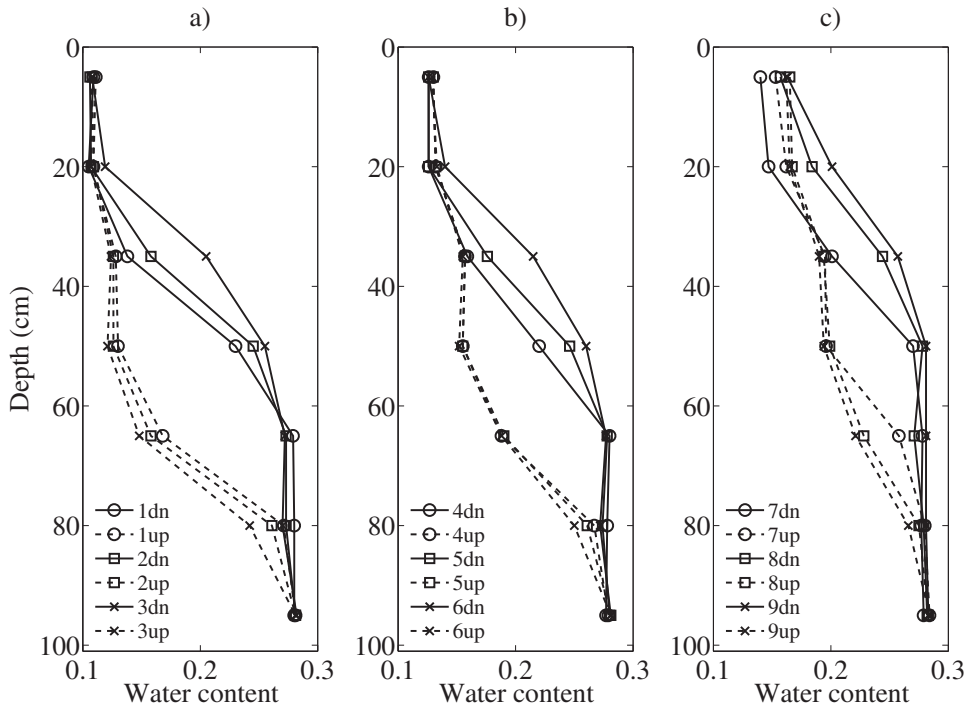

Figure 4. Measured water content profiles during falling water table tests (drying) and rising water table tests (wetting).

number 8 was located in a continuously saturated portion of the column. In Figure 4, 1dn and 1up denote test 1 with water table moving down and up, respectively. Moisture profile plots for "up" tests are shown with dashed lines.

Childs and Poulovassilis [1962] developed an analytical expression for the steady state moisture profile above a constant speed falling water table in the case of a constant applied infiltration flux. Measured water content profiles in the case of a falling water table were compared against the analytical solution by *Childs and Poulovassilis* [1962] and that result is shown in Figure 5. The agreement between measurements and analytical solutions is fair. The analytical solution of *Childs and Poulovassilis* [1962] assumed $\partial\psi/\partial z=0$ above the water table and it significantly underestimated the height of the capillary fringe in the case of a larger applied surface fluxes (tests 7–9). Another reason for the difference between measurements and analytical solution is that a steady state moisture profile was not reached.

Hysteresis effects were observed in the transient water content profiles. For the same suction head, the water content obtained from a falling water table (drying) was generally greater than that in the case of a rising water table (wetting). Note in Figure 4 that both drying curves (solid lines) and wetting curves (dashed lines) were measured during transient conditions, not steady state. Measured transient scanning curves using three capillary head sensors and TDR 2, 3, 6, for tests with the slowest water table velocity (13 cm/h) are shown in Figure 6.

The results in Figure 6 show that the relationship between water content and suction head varies at different locations depending on wetting/drying, water table velocity, and the applied surface flux. The shape and size of the scanning curves change with changing surface flux as explained by equation (B4). With increasing surface flux, the retention curves change similarly to decreasing either the curve fitting parameter n in the *Van Genuchten* [1980] model or the pore distribution index λ in the *Brooks and Corey* [1964] model.

In numerical tests of both the improved T-O and RE solvers, a fully saturated domain was used as the initial condition and the measured water level in the constant head tank was used as the lower head boundary condition. Hysteresis effects and air entrapment were not considered in our numerical simulations. The calibrated van Genuchten parameters used for the Wedron sand in tests 1–6 for simulations with both the T-O and Hydrus-1D solvers were

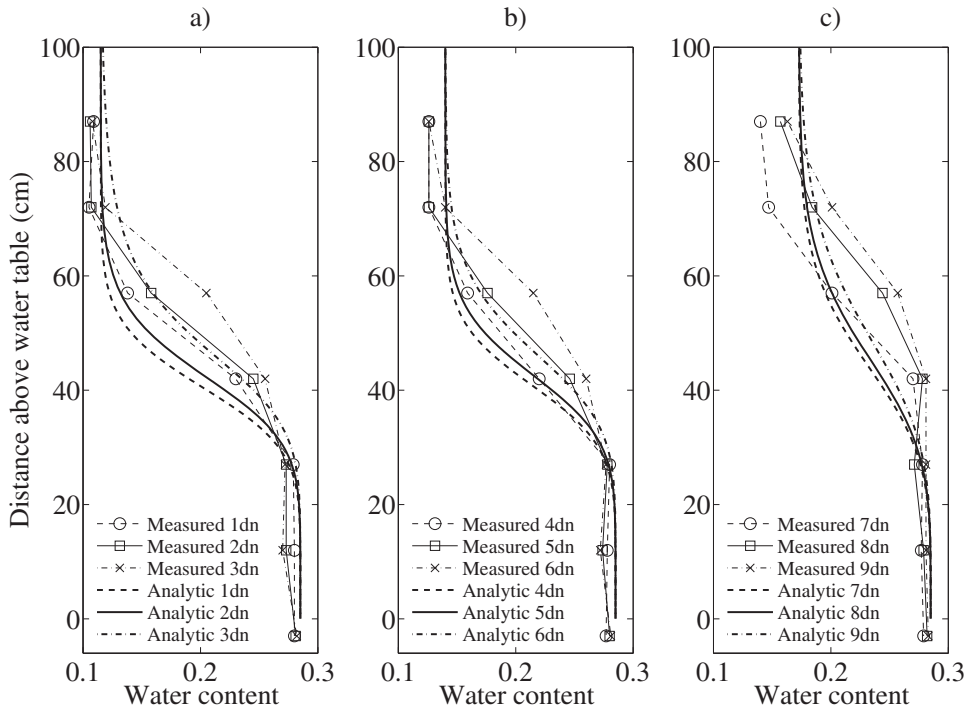

Figure 5. Comparison of measured and analytic [*Childs and Polouvassilis*, 1962] steady state moisture profiles.

$$\theta_r = 0.02, \quad \theta_e = 0.285, \quad n = 6.5, \quad \alpha = 0.025\,\text{cm}^{-1}, \quad K_s = 60\,\text{cm/h}. \tag{4}$$

Measured and simulated evolutions of water content at each TDR are shown in Figure 7 for tests 1–3 and in Figure 8 for tests 4 through 6. In Figure 7 results for tests 1–3 are plotted in sequence with an input flux of 2.356 cm/h, and water table velocities of 13.2, 27.6, and 55.2 cm h^{-1}, for tests 1, 2, and 3, respectively.

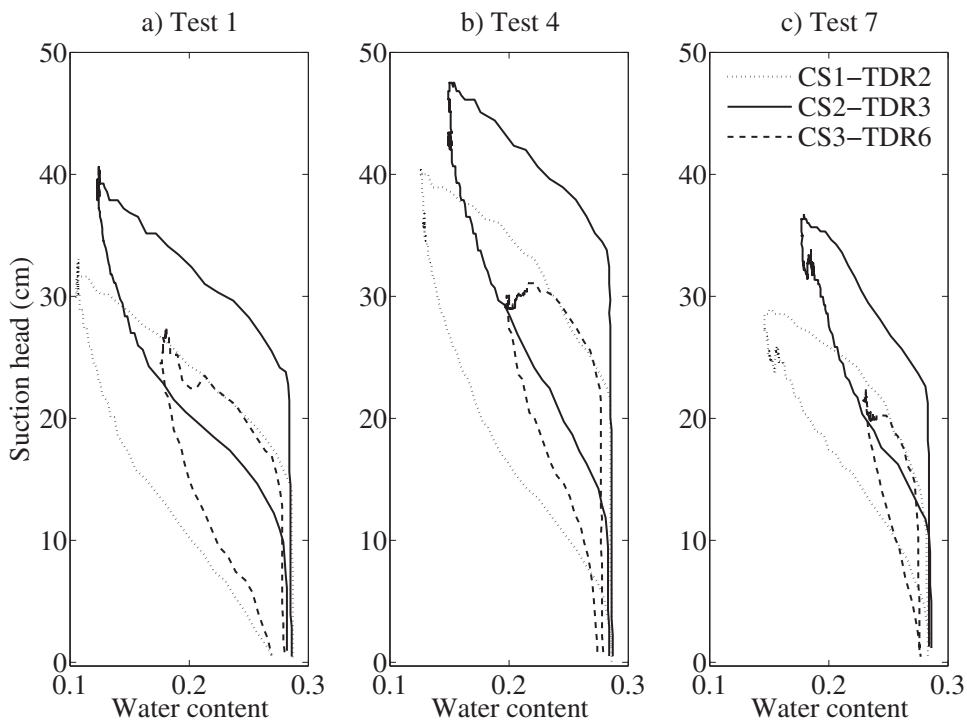

Figure 6. Measured transient scanning curves for Tests 1, 4, and 7.

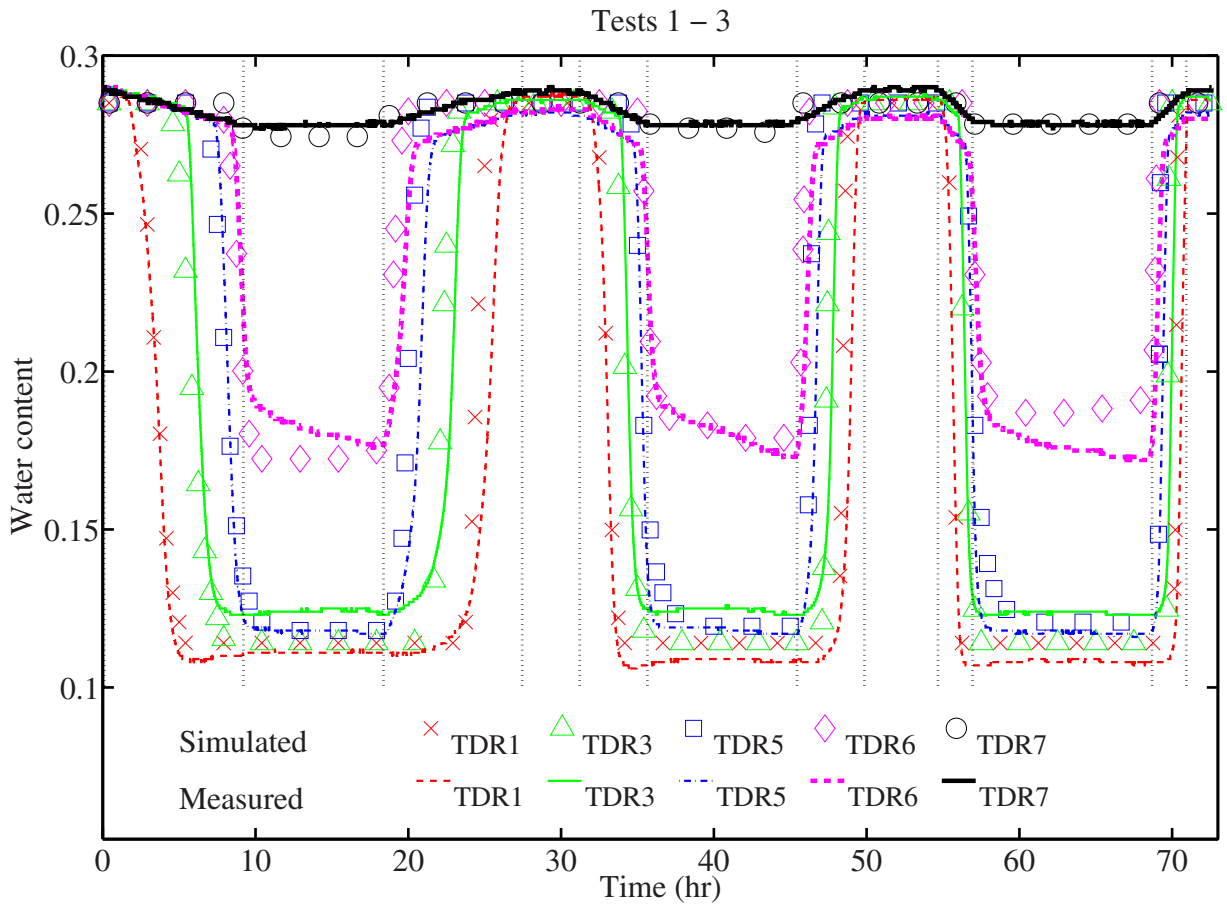

Figure 7. Measured and improved T-O simulated water content for Tests 1–3.

Results from tests 4–6 plotted in Figure 8 have an input flux of 4.71 cm h^{-1} for the same water table velocities, respectively. The measured water contents are plotted using lines, while simulated results using the described T-O method are shown using symbols. Vertical dotted lines are used to denote the start and finish times of water table motion for each test.

The simulations using the improved T-O method agreed well with the measurements, more so in the case of a falling water table. The differences between observations and the performance of the modified T-O method may be attributed to three main factors. First, a well-defined fully saturated initial condition can be used in the simulation prior to the falling of water table, while in the rising water table stage the initial water content conditions were not be fully known. Second, hysteresis effects were not considered which may cause difference in the performance of T-O method for falling and rising water table. Third, slight heterogeneity in fully saturated water content was observed among the seven TDR locations. The measured low water contents when water table was at its lowest position are also different for TDRs 1–5, while the simulated results indicate the same water content at these TDR locations.

At the end of test 6, after more than 160 h of experiments, some minor changes were observed in the sand hydraulic properties. We speculate that these changes were due to air compression effects. The increasing flux intensity also affected the sand surface characteristics as the tests progressed. For tests 7–9 the following calibrated van Genuchten parameters were used in both the T-O and Hydrus-1D simulations, with smaller values of n and α compared against the previous values

$$\theta_r = 0.02, \quad \theta_e = 0.285, \quad n = 4.5, \quad \alpha = 0.022\,\mathrm{cm}^{-1}, \quad K_s = 60\,\mathrm{cm/h}. \tag{5}$$

Measured water content evolutions and T-O simulation results for tests 7–9 are shown in Figure 9, which all had an applied surface flux of 7.6 cm h^{-1}. Note that tests 8–9 were performed at a later time due to malfunction of the TDR system for the indicated gap in Figure 9.

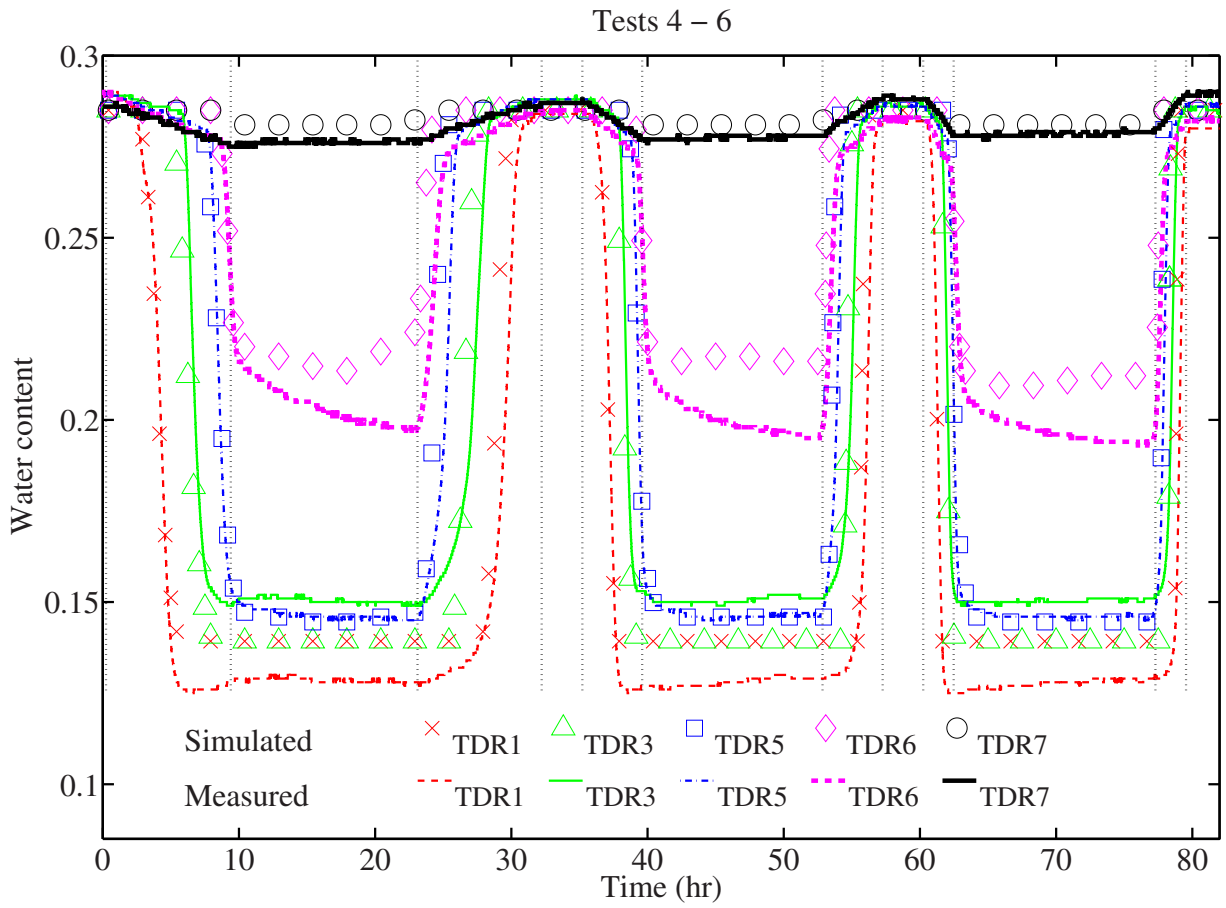

Figure 8. Measured and improved T-O simulated water content for Tests 4–6.

The performance of the T-O method was evaluated using the Nash-Sutcliffe efficiency (NSE) [*Nash and Sutcliffe*, 1970] index and percent bias (PBIAS). The NSE was computed using

$$\mathrm{NSE}=1-\frac{\sum_{i=1}^{n}\left(Y_i^{obs}-Y_i^{sim}\right)^2}{\sum_{i=1}^{n}\left(Y_i^{obs}-\bar{Y}\right)^2}. \tag{6}$$

The NSE recasts the root mean square error in a form that compares the model against the mean of the time series. The NSE ranges between 1 and $-\infty$, with 1 indicating perfect model agreement with the observations. Positive NSE values indicate that the model has more skill than the mean in representing the time series, while negative NSE values indicate the mean of the observations is better predictor than the model.

The percent bias (PBIAS) was computed using

$$\mathrm{PBIAS}=\frac{\sum_{i=1}^{n}\left(Y_i^{obs}-Y_i^{sim}\right)}{\sum_{i=1}^{n}Y_i^{obs}}\times 100\%, \tag{7}$$

where Y_i^{obs} and Y_i^{sim} are the ith observation and simulated values, $\bar{Y}$ is the mean of the observed data, and n is the total number of observations. The PBIAS indicates the tendency of a model to over or underestimate the variable of interest, and by how much, expressed as a percentage of the observed value.

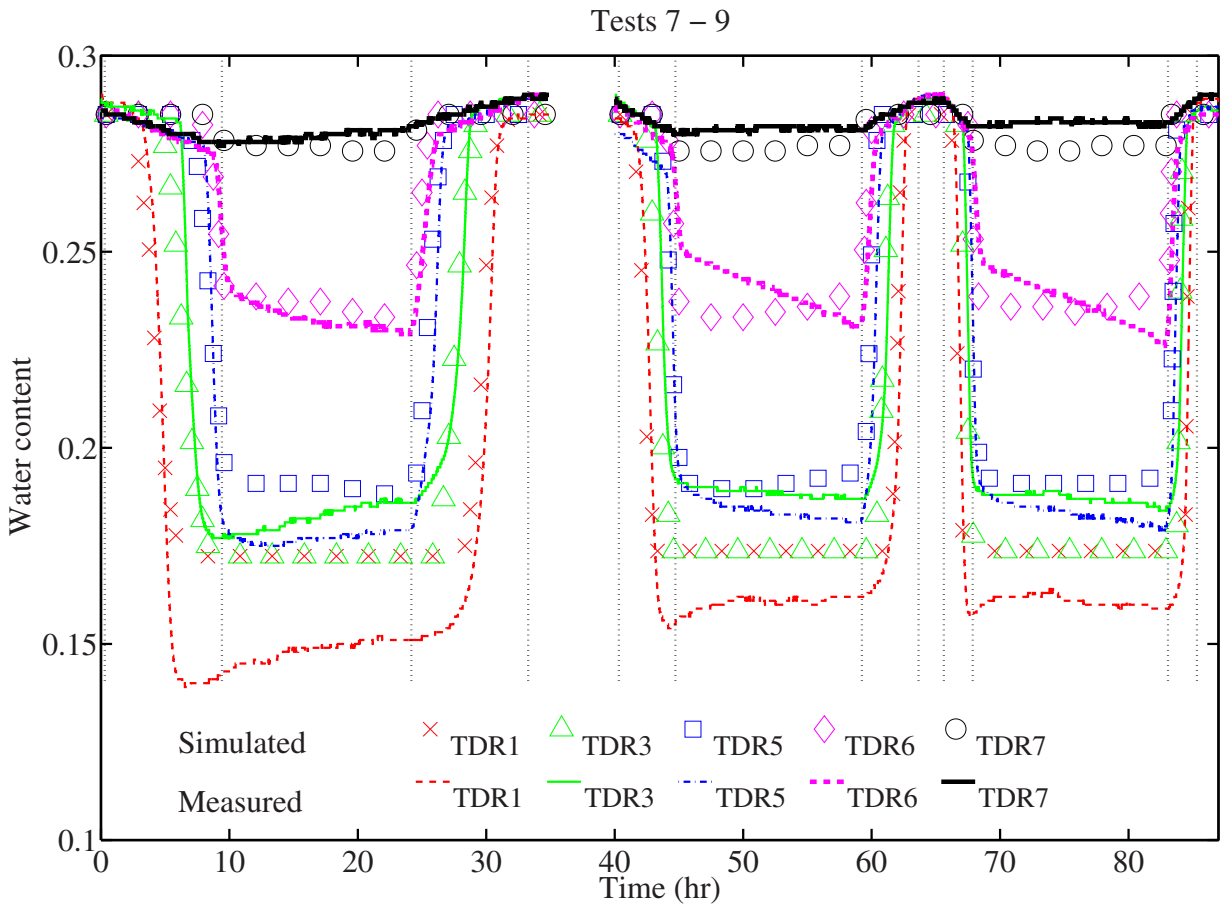

Figure 9. Measured and improved T-O simulated water content for Tests 7–9.

Model simulations can be subjectively judged as satisfactory if the NSE is >0.5 and the absolute value of PBIAS is less than 25% [*Moriasi et al.*, 2007]. As seen in Tables 2 and 3, the simulated results at TDRs 1–5 are generally satisfactory in both falling and rising water table tests. The NSE for TDRs 6 and 7 are generally below 0.5, because the series mean is a decent approximation of the behavior at these depths in the column where the water content is consistently high. The absolute PBIAS values are typically less than 7 and 1% at TDRs 6 and 7, respectively.

Table 2. Summary of NSE for T-O Numerical Predictions (−)

		Test Number								
W.T. Dir.	TDR	1	2	3	4	5	6	7	8	9
Down	1	0.99	0.99	0.99	0.98	0.98	0.98	0.87	0.89	0.89
Down	2	0.96	0.98	0.98	0.98	0.97	0.98	0.88	0.87	0.89
Down	3	0.92	0.94	0.96	0.92	0.90	0.91	0.90	0.62	0.61
Down	4	0.95	0.96	0.96	0.97	0.96	0.95	0.91	0.71	0.52
Down	5	0.96	0.93	0.84	0.98	0.97	0.94	0.89	0.52	0.59
Down	6	0.51	−0.13	−2.83	0.70	−0.14	−1.83	−0.04	−0.93	−0.19
Down	7	0.06	−0.07	0.04	−1.21	−0.58	−0.11	−1.62	−0.04	0.13
Up	1	0.75	0.60	0.03	0.84	0.74	0.51	0.90	0.95	0.90
Up	2	0.83	0.72	0.46	0.84	0.84	0.78	0.97	0.94	0.90
Up	3	0.89	0.84	0.71	0.87	0.83	0.75	0.95	0.91	0.87
Up	4	0.86	0.82	0.74	0.84	0.85	0.82	0.94	0.90	0.85
Up	5	0.76	0.74	0.66	0.73	0.77	0.76	0.90	0.78	0.75
Up	6	0.60	0.51	0.39	0.29	0.30	0.30	0.83	0.70	0.50
Up	7	0.13	0.14	0.01	−0.77	−0.06	0.12	−0.27	0.23	−0.32

Table 3. Summary of PBIAS for T-O Numerical Predictions (%)

		Test								
W.T. Dir.	TDR	1	2	3	4	5	6	7	8	9
Down	1	−2.19	−3.33	−2.63	−2.35	−1.95	−2.24	−4.54	0.98	3.01
Down	2	1.42	−0.38	−2.24	−0.29	0.41	0.83	−0.58	2.4	3.75
Down	3	5.11	3.14	1.79	4.52	4.37	3.15	3.14	5.42	4.89
Down	4	2.47	0.43	−0.56	0.24	1.00	1.24	0.79	3.18	3.33
Down	5	0.83	−2.13	−2.64	0.22	−0.05	−0.55	−0.35	−1.54	1.32
Down	6	0.72	−2.17	−3.46	−0.55	−1.94	−2.92	−0.81	−0.45	0.36
Down	7	−0.37	−0.44	−0.11	−1.33	−0.85	−0.39	−1.19	−0.34	0.09
Up	1	−9.87	−12.56	−17.53	−8.66	−10.22	−12.15	−7.23	−3.59	−5.16
Up	2	−9.22	−11.81	−17.49	−7.24	−7.36	−8.73	−2.06	−3.23	−5.02
Up	3	−2.38	−3.48	−6.3	−1.27	−1.56	−2.79	1.94	0.43	−0.83
Up	4	−5.13	−6.36	−8.25	−4.21	−3.61	−3.97	−1.49	−1.73	−3.28
Up	5	−7.35	−8.01	−9.57	−4.8	−4.77	−5.02	−1.87	−3.46	−4.56
Up	6	−4.88	−6.11	−6.98	−4.77	−5.46	−5.98	−1.00	−1.58	−2.97
Up	7	−0.27	−0.10	−0.40	−1.02	−0.45	−0.11	0.51	0.16	0.44

For comparison, the vadose zone dynamics were also simulated using the numerical solution of the RE using the Hydrus-1D program [*Simunek et al.*, 2009] using the same *Van Genuchten* [1980] parameters used in the T-O solution. Hydrus-1D solves the RE for variably saturated water flow based on finite element method with mass conservative implicit iterative scheme [*Celia et al.*, 1990]. Simulated results for tests 1–3 and 7–9 are shown in Figures 10 and 11 together with the observations for qualitative comparison against the T-O simulation results shown in Figure 12.

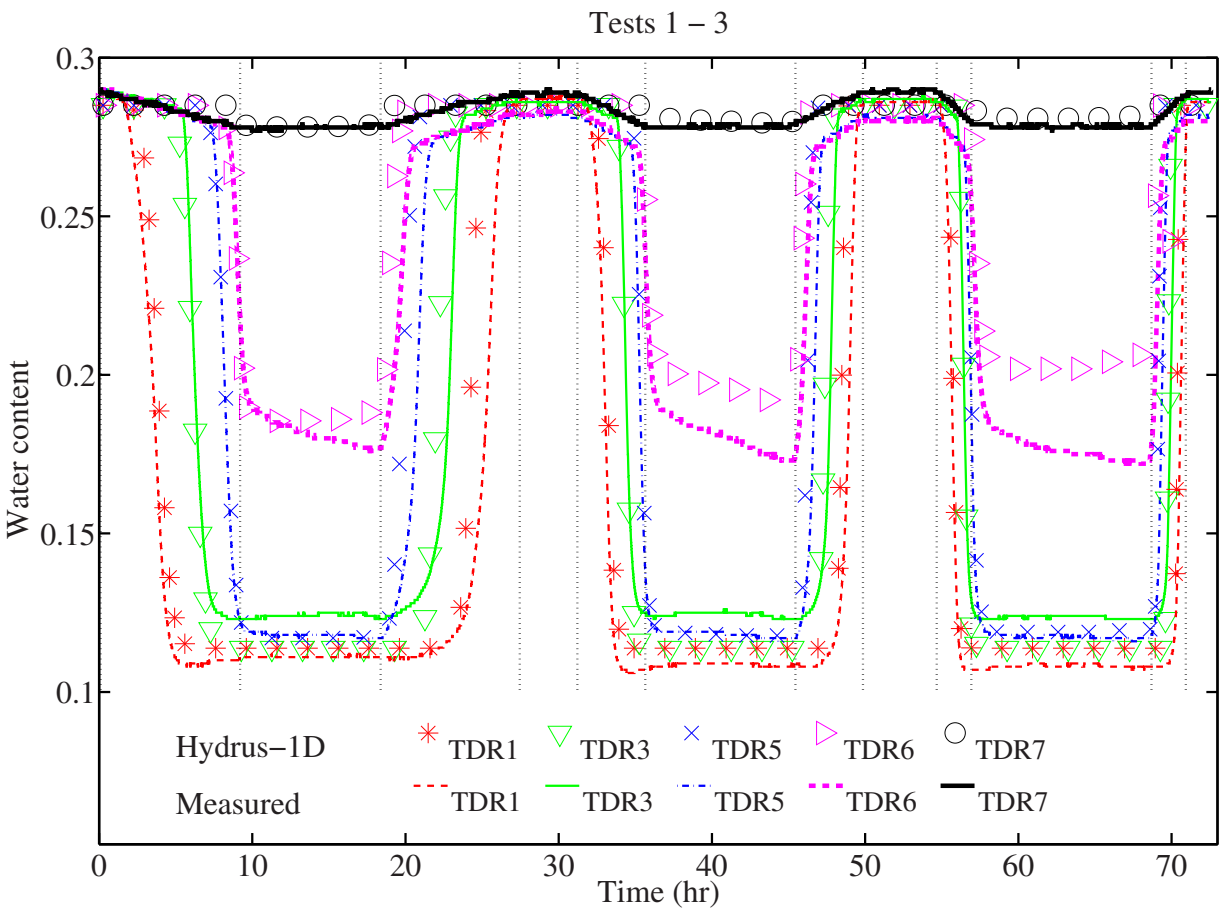

Figure 10. Measured and Hydrus-1D simulated water content for Tests 1–3.

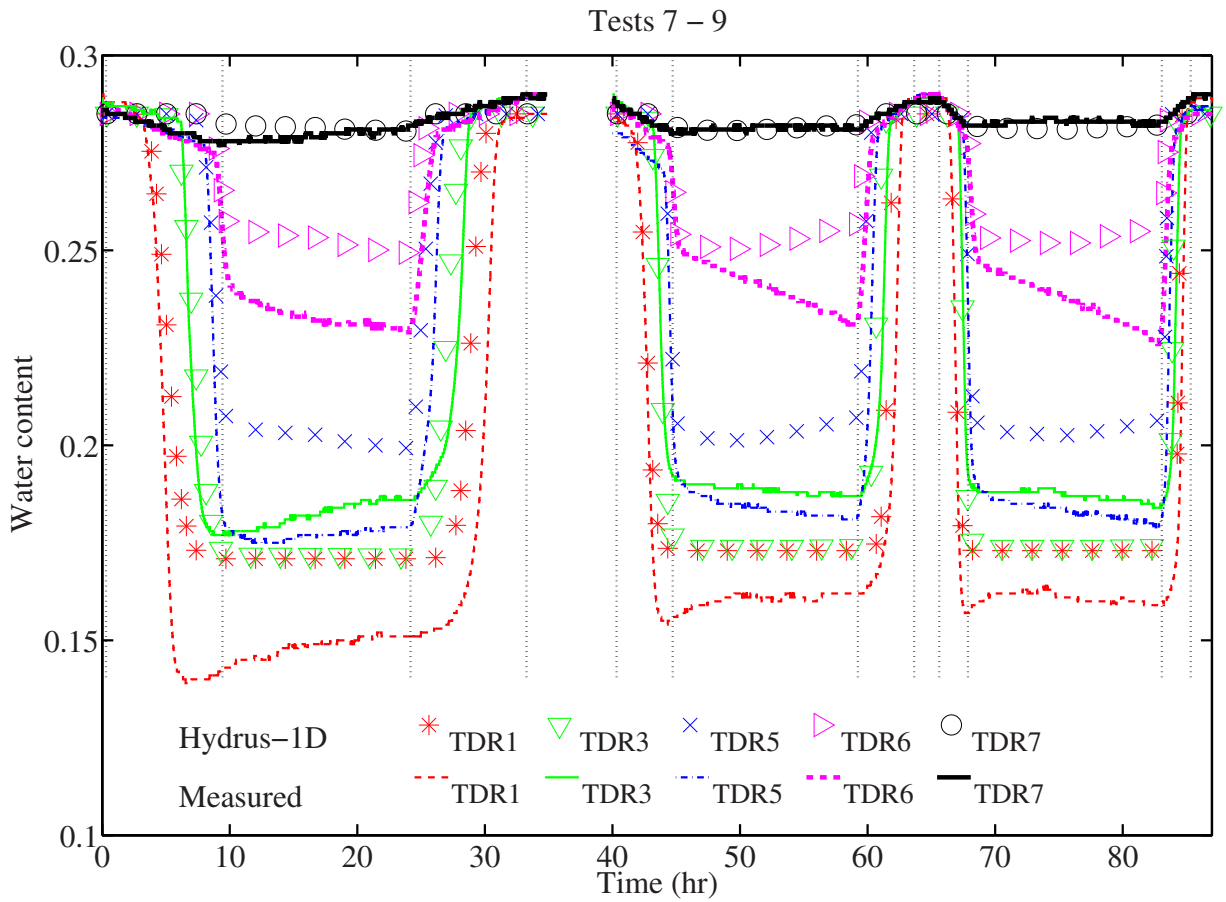

Figure 11. Measured and Hydrus-1D simulated water content for Tests 7–9.

The Hydrus-1D simulation NSE and PBIAS values are listed in Tables 4 and 5. Figure 12a shows NSE > 0 for T-O plotted against Hydrus-1D and Figure 12b shows the absolute value of PBIAS for T-O compared against Hydrus-1D. Results in Figure 12a show that in Both Hydrus-1D and T-O method have quite similar performance with NSE values nearer 1.0 during falling water table tests. The lower NSE values for the rising water table tests might likely be due to initial condition uncertainty. However, the majority of the rising water table tests with NSE > 0.5 occur above the line of perfect agreement, which indicates that on average in the case of rising water table, the NSE is higher in the case of the T-O method. Figure 12b shows that the |PBIAS| is smaller for the T-O method for most tests, because the majority of those points lie below the line of perfect agreement, which indicates lower |PBIAS| values for the T-O method. In terms of both NSE and |PBIAS|,

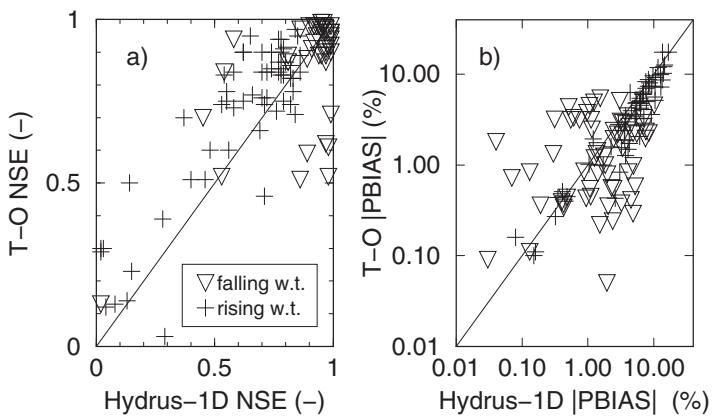

Figure 12. Relative performance measures for the T-O method and Hydrus-1D: (a) Nash-Sutcliffe efficiencies and (b) absolute percentage bias. Both plots show the 1:1 line. The symbols and legend indicate direction of water table motion for both plots.

Table 4. Summary of NSE for Hydrus-1D Predictions (−)

		Test Number								
W.T. Dir.	TDR	1	2	3	4	5	6	7	8	9
Down	1	0.96	0.95	0.95	0.92	0.93	0.92	0.81	0.94	0.95
Down	2	0.99	0.99	0.96	0.94	0.95	0.96	0.89	0.97	0.97
Down	3	0.98	0.99	0.99	0.99	0.99	0.97	0.97	0.97	0.98
Down	4	0.99	0.99	0.96	0.97	0.97	0.93	0.91	0.99	0.98
Down	5	0.99	0.92	0.54	0.9	0.86	0.58	0.81	0.53	0.89
Down	6	0.86	−0.37	−3.99	0.45	−0.82	−2.91	0.00	−0.23	0.29
Down	7	−0.05	−0.17	−0.01	−1.27	−0.64	−0.14	−1.95	−0.29	0.02
Up	1	0.62	0.56	0.29	0.58	0.53	0.46	0.62	0.65	0.62
Up	2	0.79	0.76	0.71	0.7	0.77	0.83	0.84	0.77	0.78
Up	3	0.86	0.86	0.84	0.77	0.78	0.79	0.85	0.79	0.8
Up	4	0.82	0.82	0.82	0.72	0.78	0.83	0.78	0.74	0.74
Up	5	0.7	0.71	0.69	0.58	0.66	0.72	0.7	0.55	0.55
Up	6	0.48	0.4	0.28	0.02	0.02	0.03	0.54	0.37	0.14
Up	7	0.08	0.13	−0.06	−0.85	−0.15	0.04	−0.11	0.15	−0.12

Table 5. Summary of PBIAS for Hydrus-1D Predictions (%)

		Test								
W.T. Dir.	TDR	1	2	3	4	5	6	7	8	9
Down	1	−5.56	−7.04	−7.01	−7.59	−7.56	−8.39	−10.15	−4.93	−3.12
Down	2	−1.39	−3.22	−4.83	−4.83	−4.49	−4.16	−5.22	−2.46	−0.97
Down	3	3.05	1.12	0.04	1.06	0.51	−0.75	−0.55	1.54	1.24
Down	4	1.15	−0.94	−2.28	−2.39	−1.84	−1.76	−1.97	0.31	0.61
Down	5	−0.13	−3.38	−4.24	−1.51	−1.94	−2.45	−2.04	−3.37	−0.3
Down	6	0.07	−2.84	−3.99	−1.07	−2.47	−3.37	−1.41	−1.11	−0.19
Down	7	−0.43	−0.48	−0.13	−1.35	−0.87	−0.4	−1.26	−0.43	0.03
Up	1	−12.64	−14.62	−16.8	−13.39	−13.97	−14.16	−12.84	−9.22	−10.55
Up	2	−10.59	−11.58	−13.7	−10.44	−9.3	−8.28	−6.13	−7.08	−7.68
Up	3	−3.58	−3.74	−4.41	−3.72	−3.24	−2.92	−1.2	−2.59	−3.04
Up	4	−6.31	−6.98	−7.6	−6.28	−5.21	−4.6	−4.09	−4.27	−5.47
Up	5	−8.36	−8.74	−9.72	−6.38	−6.21	−6.16	−3.61	−5.2	−6.3
Up	6	−5.53	−6.76	−7.63	−5.36	−6.19	−6.91	−1.7	−2.24	−3.72
Up	7	−0.32	−0.15	−0.45	−1.04	−0.48	−0.16	0.41	0.08	0.35

Table 6. Measured and Simulated Deponding (t_{dp}) and Ponding Times (t_p), and the Absolute Value of These Time Differences (h)

	Observed		Hydrus-1D		T-O Method		Hydrus-1D		T-O Method	
Test	t_{dp}	t_p	t_{dp}	t_p	t_{dp}	t_p	$\lvert\Delta t_{dp}\rvert$	$\lvert\Delta t_p\rvert$	$\lvert\Delta t_{dp}\rvert$	$\lvert\Delta t_p\rvert$
1	0.46	8.84	0.54	8.53	0.48	8.52	0.08	0.31	0.02	0.32
2	0.35	4.51	0.35	4.12	0.30	4.10	0.00	0.39	0.05	0.41
3	0.25	2.43	0.21	2.04	0.18	2.06	0.04	0.39	0.07	0.37
4	0.99	8.64	1.30	7.95	1.26	7.94	0.31	0.69	0.27	0.70
5	0.76	4.27	0.62	3.86	0.56	3.53	0.14	0.41	0.20	0.74
6	0.43	2.24	0.32	1.99	0.28	1.82	0.11	0.25	0.15	0.42
7	1.60	7.79	1.58	7.65	1.19	7.52	0.02	0.14	0.41	0.27
8	1.07	3.59	0.74	3.66	0.50	3.64	0.33	0.07	0.57	0.05
9	0.56	1.86	0.41	1.86	0.29	1.83	0.15	0.00	0.27	0.03
					Averages:		0.13	0.29	0.22	0.37

a greater percentage of the T-O solutions have NSE > 0.5 than the Hydrus-1D solutions, and the T-O solution on average has a smaller absolute bias.

Measured and simulated deponding time from the start of falling water table (t_{dp}) and ponding time when the water table was rising (t_p) are listed in Table 6 for tests 1–9. The differences between measured and simulated deponding and ponding times are generally smaller in the Hydrus-1D simulations than with the

T-O method. There is some correlation between the time differences for the two numerical methods. Tests 4 up, 4 down, 5 up, and 8 down have considerably larger time errors for both numerical methods than other tests.

5. Conclusions

In this study, the finite water content *Talbot and Ogden* [2008] vadose zone simulation method was improved and modified to include groundwater table dynamics and validated using data collected in a column experiment patterned after that by *Childs and Poulovassilis* [1962] with moving water table and specified flux upper boundary conditions. The improved T-O formulation was found to agree satisfactorily with experimental data for the evolution of soil water content above a moving water table. The ordinary differential equation T-O method was also compared with the Hydrus-1D numerical solutions of the *Richards* [1931] partial differential equation. Results showed similar performance for both methods in simulating water content evolution. The T-O method on average had higher Nash-Sutcliffe efficiencies and lower absolute bias than Hydrus-1D. Average absolute differences in predicted deponding/ponding times between measurements were 7.8/17.4 and 13.2/22.2 min for Hydrus-1D and the T-O method, respectively. The improved T-O method was able to predict general features of vadose zone dynamics with moving water table and surface infiltration using an explicit, mass-conservative formulation. The advantages of the ODE T-O formulation are that it is numerically simple, explicit, and guaranteed to converge and conserve mass. These properties make the improved T-O method presented in this paper a robust and computationally efficient alternative to the numerical solution of the *Richards* [1931] equation, which is occasionally subject to stability and mass conservation limitations that affect its robustness and computational efficiency in the context of hydrological modeling.

Appendix A: Derivation of Finite Water-Content Vadose Zone Moisture Dynamic Equation in Response to Groundwater Table Motion

This derivation is a partial excerpt of the derivation presented in *Ogden et al*. [2015]. It is shown here to provide theoretical underpinning for the groundwater wetting front dynamical equation (3). The reader is reminded that in the 1-D finite water-content discretization there is only one spatial dimension, *z*, and that the θ-dimension is conceptual, with no spatial dimension.

Mass conservation of one-dimensional vertically flowing incompressible water in an unsaturated incompressible porous media without internal sources or sinks is given by

$$\frac{\partial \theta}{\partial t}+\frac{\partial q}{\partial z}=0, \tag{A1}$$

where z is defined as positive downward and the flux q (LT^{-1}) can be described using unsaturated Darcy's law

$$q=-K(\theta)\frac{\partial \psi(\theta)}{\partial z}+K(\theta). \tag{A2}$$

Substitution of equation (A2) into equation (A1) gives the 1-D *Richards* [1931] partial differential equation in mixed form. Our solution does not take that approach. Rather, we use chain rule operations to transform equation (A1) into another form where θ and *z* change roles, with *z* becoming the dependent variable and θ the independent variable along with time *t*. The cyclic chain rule is used to describe the first term in equation (A1) [*Philip*, 1969, equation (51); *Wilson*, 1974, equation (3.4)]

$$\left(\frac{\partial \theta}{\partial t}\right)_z=-\frac{(\partial \theta/\partial z)_t}{(\partial t/\partial z)_\theta}=-\frac{(\partial z/\partial t)_\theta}{(\partial z/\partial \theta)_t}, \tag{A3}$$

while the normal chain rule is used to describe the second term in equation (A1)

$$\left(\frac{\partial q}{\partial z}\right)_t=\left(\frac{\partial q}{\partial \theta}\right)_t\left(\frac{\partial \theta}{\partial z}\right)_t. \tag{A4}$$

Substitution of equations (A3) and (A4) into equation (A1), $(\partial\theta/\partial z)_t$ and eliminating like terms yields

$$\left(\frac{\partial z}{\partial t}\right)_\theta = \left(\frac{\partial q}{\partial \theta}\right)_t. \tag{A5}$$

Substitution of the flux term q (equation (A2) into equation (A5)) and evaluating the term on the right-hand side of equation (A5) gives

$$\frac{\partial q}{\partial \theta} = \frac{\partial}{\partial \theta}\left[K(\theta)\left(1 - \frac{\partial \psi(\theta)}{\partial z}\right)\right] = \frac{\partial K(\theta)}{\partial \theta}\left(1 - \frac{\partial \psi(\theta)}{\partial z}\right) - K(\theta)\frac{\partial^2 \psi(\theta)}{\partial z \partial \theta}. \tag{A6}$$

At static equilibrium, $\partial\psi/\partial z = 1$ in the case of a groundwater front and the right-hand side of equation (A6) is zero because $\partial/\partial\theta\ (\partial\psi/\partial z) = 0$. In the case of a moving water table, equilibrium is most nearly sustained in the right-most bins where the conductivity is highest. However, the occurrence of this condition requires that the velocity of the water table V_w (L T^{-1}) be somewhat less than the saturated hydraulic conductivity K_s. In the case of bins on the left where there are likely significant deviations from equilibrium conditions, the cross partial-derivative term is multiplied by a very small value of $K(\theta)$, which makes this term small. The results shown in this paper support our assumption that this cross partial-derivative term is either zero or small and negligible when $V_w \leq 0.92\ K_s$. The resulting 1-D flux equation is therefore the remaining portion of equation (A6)

$$\left(\frac{dz}{dt}\right)_\theta = \frac{\partial K(\theta)}{\partial \theta}\left(1 - \frac{\partial \psi(\theta)}{\partial z}\right). \tag{A7}$$

One way to solve equation (A7) is to solve it for $q(\theta,t)$ and $z(\theta,t)$ by integration [*Parlange*, 1971; *Wilson*, 1974]

$$\int \frac{\partial q}{\partial \theta} d\theta = \int \frac{\partial z}{\partial t} d\theta, \tag{A8}$$

by inserting equation (A7) on the right-hand side. Instead, by adopting a finite water-content discretization in θ we replace the integrals with summations

$$\sum_{j=1}^{N}\left[\frac{\partial q}{\partial \theta}\right]_j \Delta\theta = \sum_{j=1}^{N}\left[\frac{\partial z}{\partial t}\right]_j \Delta\theta. \tag{A9}$$

Summations are performed across the uniform finite water-content bins where N is the total number of bins and $j \leq N$ is the bin index. With this approach, the conservation equation for each bin j is

$$\left[\frac{\partial q}{\partial \theta}\right]_j = \left[\frac{\partial z}{\partial t}\right]_j. \tag{A10}$$

In the case of a dynamic groundwater table, the water level in each bin will rise or fall relative to the difference between the top elevation of the water in a bin, which we call a "groundwater front" (see Figure 2), and the hydrostatic level for a given water table depth Z_w. In the case of groundwater fronts, capillarity acts in the upward ($-z$) direction opposite gravity. With reference to Figure 2, flow to satisfy the groundwater front due to capillary rise in the jth bin can only travel through the pore space (not physical space) between θ_j and θ_i. In this case, the partial derivative term $\partial K(\theta)/\partial\theta$ in equation (A7) is replaced by

$$\frac{\partial K(\theta)}{\partial \theta} = \frac{K(\theta_j) - K(\theta_i)}{\theta_j - \theta_i}. \tag{A11}$$

Notice that this is the average hydraulic conductivity between θ_j and θ_i per unit available pore space and represents the ability of gravity to move water between θ_j and θ_i per unit available pore space.

The partial derivative term in unsaturated Darcy's law (equation (A2)), $\partial\psi(\theta)/\partial z$ represents the capillary gradient in bin j. With a change in variable $dz = -dh$, where h is the distance from the water table up to the wetting front, this term is replaced by

$$\frac{\partial \psi(\theta)}{\partial z} = \frac{|\psi(\theta_j)|}{h_j}, \tag{A12}$$

which is the capillary gradient in the jth bin, and equation (A7) becomes

$$\frac{dh_j}{dt} = \frac{K(\theta_j) - K(\theta_i)}{\theta_j - \theta_i}\left(\frac{|\psi(\theta_j)|}{h_j} - 1\right). \tag{A13}$$

Note that in equation (A13), when the capillary rise h_j is equal to the capillarity of the jth bin, $\psi(\theta_j)$, the water in this bin is in equilibrium and $dh_j/dt = 0$.

In summary, through a hodograph transformation followed by discretization in θ we have used the Method of Lines (MOL) [*Liskovets*, 1965; *Hamdi et al*., 2007] to convert the partial derivative form of the RE into a solvable ODE (equation (A13)) that describes the dynamics of soil moisture above a dynamic water table in a homogeneous, incompressible, unsaturated porous media.

This new method is advective, without an explicit representation of diffusion, which necessitates a separate capillary relaxation step. The finite water-content simulation approach is a two-step process, involving calculations of front advance, followed by capillary relaxation. In the case of groundwater fronts using equation (A13), higher velocities in bins to the right can result in an imbalanced profile. *Smith* [1983] called these shock fronts. We posit that these shocks are dissipated by capillary relaxation, which involves spontaneous zero-dimensional transport of water from regions of lower capillarity to regions of higher capillarity at the pore scale in a free-energy minimization process that produces no advection beyond the REV scale [*Moebius et al*., 2012]. In the case of infiltration or groundwater fronts, this is equivalent to numerically sorting either the h_j values, and putting them from maximum to minimum depth from left to right (higher ψ to lower ψ). When implemented correctly, the process of capillary relaxation conserves mass perfectly and does not cause advection.

Appendix B: Effect of Constant Applied Surface Flux on Groundwater Front Capillary Rise

In our experimental apparatus with an applied constant surface flux, the groundwater wetting front profile is not only affected by the water table motion, but also by the infiltration flux [*Smith and Hebbert*, 1983]. Assuming a constant surface flux $q_{in} < K_s$ with fixed water table at steady state, the unsaturated Darcy's flux gives

$$q_{in} = -K(\theta)\left(\frac{\partial\psi}{\partial z} - 1\right), \tag{B1}$$

which can be written as

$$\frac{\partial\psi}{\partial z} = 1 - \frac{q_{in}}{K(\theta)}. \tag{B2}$$

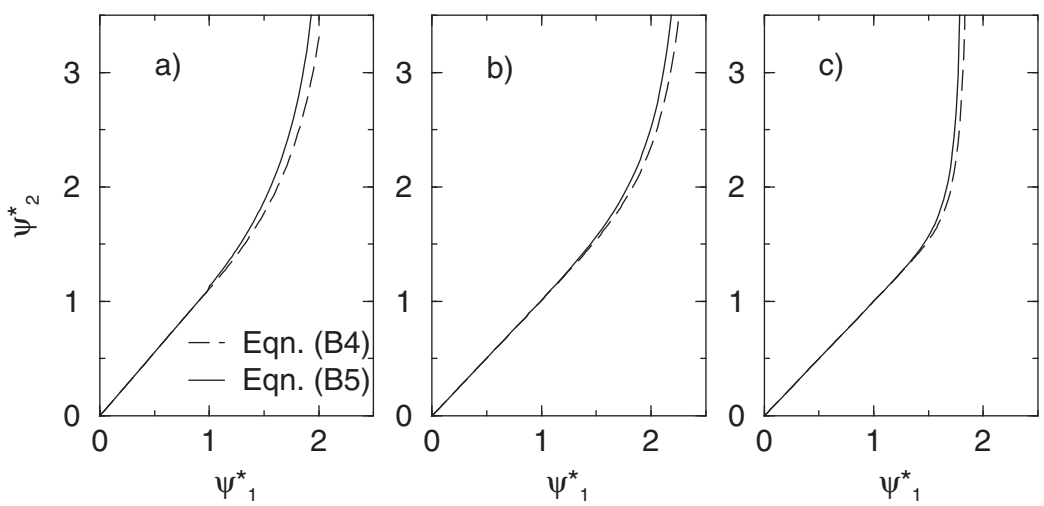

Figure B1. Dynamic capillary height ψ^*_2 versus hydrostatic capillary height ψ^*_1 for (a) clay, (b) silt loam, and (c) sand loam, comparing equation (B4) with equation (B5).

Table B1. Soil Parameters and Normalized Infiltration Rate [after *Zhu and Mohanty*, 2002]

Soil Type	K_s (cm h^{-1})	$\lvert\psi_b\rvert$ (cm)	β	$q_{in}\,K_s^{-1}$
Clay	0.122	90.09	3.30	0.1
Silt loam	1.22	45.05	5.64	0.01
Sand loam	12.2	25.0	11.88	0.001

Assuming that in the capillary fringe the media is saturated and the water pressure is equal to the bubbling pressure as in *Brooks and Corey* [1964] model, the height of the capillary fringe becomes

$$z_f = \frac{|\psi_b|}{1-q_{in}/K_s}. \tag{B3}$$

In the same way, the hydrostatic groundwater wetting front (capillary height) above the static water table can be approximated using

$$|\psi'(\theta)| = \frac{|\psi_b|}{1-\frac{q_{in}}{K_s}} + \frac{|\psi(\theta)|-|\psi_b|}{1-\frac{q_{in}}{2K(\theta)}-\frac{q_{in}}{2K_s}}. \tag{B4}$$

Note that the capillary height increases significantly and nonlinearly as q_{in} approaches K_s, and the capillary height curve is the same as retention curve when q_{in} is zero. If the van Genuchten model is used, the bubbling pressure can be approximated using the parameter equivalence relationship given by *Morel-Seytoux et al*. [1996].

The empirical finding in equation (B4) was compared against the more complete and complex analytical solution of *Zhu and Mohanty* [2002]

$$|\psi'(\theta)| = \frac{\beta|\psi_b|q_{in}/K_s}{(1-q_{in}/K_s)(1+\beta)}\sum_{j=0}^{\infty} e_j + |\psi(\theta)|\sum_{j=0}^{\infty} f_j, \tag{B5}$$

where $\beta=3\lambda+2$, λ is the *Brooks and Corey* [1964] pore size distribution index,

$$\begin{aligned} &e_0=1;\\ &e_j=\frac{(j-1+1/\beta)q_{in}/K_s}{j+1+1/\beta}e_{j-1}, j>=1; \end{aligned} \tag{B6}$$

and

$$\begin{aligned} &f_0=1;\\ &f_j=\frac{(j-1+1/\beta)s}{(j+1+1/\beta)(1+s)}f_{j-1}, j>=1;\\ &s=\left[1-q_{in}/K_s(\psi/\psi_b)^{\beta}\right]^{-1}-1. \end{aligned} \tag{B7}$$

We tested equations (B4) and (B5) on three soil textures as used by *Zhu and Mohanty* [2002]. The properties of these three soils are listed in Table B1. The hydrostatic capillary height versus capillary profiles are shown in Figure B1 using normalized capillarities $\psi^*_1=\psi\,\psi_b^{-1}$ and $\psi^*_2=\psi'\psi_b^{-1}$, for (a) clay, (b) silt loam, and (c) sand loam soil textures. The approximated solution from equation (B4) agreed well with the analytical solution (equation (B5)) at low pressure head, although equation (B4) very slightly underestimated the hydrostatic capillary height ψ^*_1.

Acknowledgments
The data from the column experiment are available through the WyCEHG database maintained by the University of Wyoming: http://wycehg.wygisc.org/content/map. On the clickable data discovery map, this data set is associated with the campus of the University of Wyoming in Laramie. The data set is stored under the name "CI-Water." This research was funded by the US National Science Foundation, EPSCoR program, through cooperative agreement EPS-1135483 to the University of Wyoming and the CI-WATER project. Edward Kempema and Mike Schilt assisted with apparatus setup. We appreciate the assistance of Scott Jones and Bill Mace of Utah State University for providing the acrylic column, TDR probes, Wedron sand, and their guidance in setting up the experiment. John L. Wilson of New Mexico Tech suggested that there might be more to the T-O method than an "approximate" solution of the Richards equation, contributed to and verified the derivation given in Appendix A. We are very grateful for review comments by Morteza Sadeghi, another anonymous reviewer, and Editor Graham Sander, all of whom improved this manuscript.

References

Abbott, M. B., J. C. Bathhurst, J. A. Cunge, P. E. O'Connell, and J. Rasmussen (1986), An introduction to the European Hydrological System – Systeme Hydrologique Europeen, "SHE" 1: History and philosophy of a physically-based, distributed modelling system, *J. Hydrol.*, *87*(1–2), 45–59.

Brooks, R. H., and A. T. Corey (1964), Hydraulic properties of porous media, *Hydrol. Pap. 3*, Colo. State Univ., Fort Collins.

Cartwright, N. (2014), Moisture-pressure dynamics above an oscillating water table, *J. Hydrol.*, *512*, 442–446.

Celia, M. A., E. T. Bouloutas, and R. L. Zarba (1990), A general mass-conservative numerical solution for the unsaturated flow equation, *Water Resour. Res.*, *26*(7), 1483–1496.

Childs, E. C., and A. Poulovassilis (1962), The moisture profile above a moving water table, *Soil Sci. J.*, *13*(2), 271–285.

Downer, C. W., and F. L. Ogden (2004a), GSSHA: Model to simulate diverse stream flow producing processes, *J. Hydrol. Eng.*, *9*(3), 161–174.

Downer, C. W., and F. L. Ogden (2004b), Appropriate vertical discretization of Richards' equation for two-dimensional watershed-scale modeling, *Hydrol. Processes*, *18*(1), 1–22.
Green, W. H., and G. A. Ampt (1911), Studies on soil physics, 1. The flow of air and water through soils, *J. Agric. Sci.*, *4*(1), 1–24.
Hamdi, S., W. E. Schiesser, and G. W. Griffiths (2007), Method of lines, *Scholarpedia*, *2*(7), 2859. doi:10.4249/scholarpedia.2859.
He, Z., W. Wu, and S. S. Wang (2008), Coupled finite-volume model for 2D surface and 3D subsurface flows, *J. Hydrol. Eng.*, *13*(9), 835–845.
Hinz, C. (1998), Analysis of unsaturated/saturated water flow near a fluctuating water table, *J. Contam. Hydrol.*, *33*(1), 59–80.
Lai, W., F. L. Ogden, R. C. Steinke, and C. A. Talbot (2015), An efficient and guaranteed stable numerical method for continuous infiltration and redistribution with a shallow dynamic water table, *Water Resour. Res.*, *51*, doi:10.1002/2014WR016487.
Lehmann, P., F. Stauffer, C. Hinz, O. Dury, and H. Fluhler (1998), Effect of hysteresis on water flow in a sand column with a fluctuating capillary fringe, *J. Contam. Hydrol.*, *33*(1), 81–100.
Liskovets, O. A. (1965), The method of lines, *Differ. Equations*, *1*(12), 1308–1323.
Moebius, F., D. Canone, and D. Or (2012), Characteristics of acoustic emissions induced by fluid front displacement in porous media, *Water Resour. Res.*, *48*(11), W11507, doi:10.1029/2012WR012525.
Morel-Seytoux, H. J., P. D. Meyer, M. Nachabe, J. Tourna, J., M. T. van Genuchten, and R. J. Lenhard (1996), Parameter equivalence for the Brooks-Corey and van Genuchten soil characteristics: Preserving the effective capillary drive, *Water Resour. Res.*, *32*(5), 1251–1258.
Moriasi, D. N., J. G. Arnold, M. W. Van Liew, R. L. Bingner, R. D. Harmel, and T. L. Veith (2007), Model evaluation guidelines for systematic quantification of accuracy in watershed simulations, *Trans. ASABE*, *50*(3), 885–900.
Nash, J. E., and J. V. Sutcliffe (1970), River flow forecasting through conceptual models, part I—A discussion of principles, *J. Hydrol.*, *10*(3), 282–290.
Ogden, F. L., and B. Saghafian (1997), Green and Ampt infiltration with redistribution, *J. Irrig. Drain. Eng.*, *123*(5), 386–393.
Ogden, F. L., W. Lai, R. C. Steinke, J. Zhu, C. A. Talbot, and J. L. Wilson (2015), A new general 1-D vadose zone solution method, *Water Resour. Res.*, *51*, doi:10.1002/2015WR017126.
Panday, S., and P. S. Huyakorn (2004), A fully coupled physically-based spatially-distributed model for evaluating surface/subsurface flow, *Adv. Water Resour.*, *27*(4), 361–382.
Parlange, J.-Y. (1971), Theory of water-movement in soils: 2. One-dimensional infiltration, *Soil Sci.*, *111*(3), 170–174, doi:10.1097/00010694–197103000-00004.
Philip, J. R. (1969), Theory of infiltration, *Adv. Hydrosci.*, *5*, 215–296.
Richards, L. A. (1931), Capillary conduction of liquids through porous mediums, *J. Appl. Phys.*, *1*(5), 318–333.
Schmutz, P. P., and S. L. Namikas (2013), Measurement and modeling of moisture content above an oscillating water table: Implications for beach surface moisture dynamics, *Earth Surf. Process Landforms*, *38*(11), 1317–1325.
Simunek, J., M. Sejna, H. Saito, M. Sakai, and M. T. van Genuchten (2009), The HYDRUS-1D software package for simulating the one-dimensional movement of water, heat, and multiple solutes in variably-saturated media, Dep. of Environ. Sci., Univ. of Calif. Riverside, Riverside, Calif.
Smith, R. E. (1983), Approximate soil water movement by kinematic characteristics, *Soil Sci. Soc. Am. J.*, *47*(1), 3–8.
Smith, R. E., and R. H. B. Hebbert (1983), Mathematical simulation of interdependent surface and subsurface hydrologic processes, *Water Resour. Res.*, *19*(4), 987–1001.
Talbot, C. A., and F. L. Ogden (2008), A method for computing infiltration and redistribution in a discretized moisture content domain, *Water Resour. Res.*, *44*, W08453, doi:10.1029/2008WR006815.
van Dam, J. C., and R. A. Feddes (2000), Numerical simulation of infiltration, evaporation, and shallow groundwater levels with the Richards equation, *J. Hydrol.*, *233*(1–4), 72–85.
van Dam, J. C., P. Groenendijk, R. F. Hendriks, and J. G. Kroes (2008), Advances of modeling water flow in variably saturated soils with SWAP, *Vadose Zone J.*, *7*(2), 640–653.
Van Genuchten, M. Th. (1980), A closed-form equation for predicting the hydraulic conductivity of unsaturated soils, *Soil Sci. Soc. Am. J.*, *44*(5), 892–898.
Vogel, H.-J., and O. Ippisch (2008), Estimation of a critical spatial discretization limit for solving Richards' equation at large scales, *Vadose Zone J.*, *7*(1), 112–114.
Vogel, T., M. Th. van Genuchten, and M. Cislerova (2000), Effect of the shape of the soil hydraulic functions near saturation on variably-saturated flow predictions, *Adv. Water Resour.*, *24*(2), 133–144, doi:10.1016/S0309–1708(00)00037-3.
Watson, K. K., and S. A. Awadalla (1985), Comparative study of Green and Ampt analysis for a falling water table in a homogeneous sand profile, *Water Resour. Res.*, *21*(8), 1157–1164.
Watson, K. K., and S. A. Awadalla (1986), Green and Ampt analyses for rising water table and intermittent surface flux conditions, *Water Resour. Res.*, *22*(13), 1835–1843.
Wilson, J. L. (1974), Dispersive mixing in a partially saturated porous medium, PhD dissertation, 355 pp., Dep. of Civ. Eng., Mass. Inst. of Technol., Cambridge.
Zhu, J., and B. P. Mohanty (2002), Analytical solutions for steady state vertical infiltration, *Water Resour. Res.*, *38*(8), 20–1–20-5, doi:10.1029/2001WR000398.